

Oxygenated CdS Buffer Layers Enabling High Open-Circuit Voltages in Earth-Abundant $\text{Cu}_2\text{BaSnS}_4$ Thin-Film Solar Cells

Jie Ge,* Prakash Koirala, Corey R. Grice, Paul J. Roland, Yue Yu, Xinxuan Tan, Randy J. Ellingson, Robert W. Collins, and Yanfa Yan*

Earth-abundant $\text{Cu}_2\text{BaSnS}_4$ (CBTS) thin films exhibit a wide bandgap of 2.04–2.07 eV, a high absorption coefficient $> 10^4 \text{ cm}^{-1}$, and a p-type conductivity, suitable as a top-cell absorber in tandem solar cell devices. In this work, sputtered oxygenated CdS (CdS:O) buffer layers are demonstrated to create a good p–n diode with CBTS and enable high open-circuit voltages of 0.9–1.1 V by minimizing interface recombination. The best power conversion efficiency of 2.03% is reached under AM 1.5G illumination based on the configuration of fluorine-doped SnO_2 (back contact)/CBTS/CdS:O/CdS/ZnO/aluminum-doped ZnO (front contact).

1. Introduction

Earth-abundant and air-stable thin-film materials are regarded as one promising option to meet the increasing demand for low-cost solar cell manufacturing. Earth-abundant $\text{Cu}_2\text{BaSnS}_4$ (CBTS), crystallizing into the trigonal symmetry with a space group of either $P3_1$, $P3_121$, or $P3_221$,^[1,2] has emerged as a promising low-cost solar energy material and has attracted the attention of the academic community. Its noncentrosymmetric crystal structure, along with the large atomic size differences among the constituent cation elements, endow CBTS with more beneficial defect properties for efficient photovoltaic and photoelectrochemical solar energy conversion than kesterite $\text{Cu}_2\text{ZnSnS}_4$ (CZTS).^[3,4] Its wide bandgap, $E_g \approx 2 \text{ eV}$,^[4,5] is suitable as a top-cell absorber in a tandem solar device. Tandem solar devices generally consists of two or more stacked subcells, whereby the top cell absorbs only the blue light of the solar spectrum leaving the red light to pass through and be absorbed by the bottom cell. Thus, the top-cell absorber calls for a wide bandgap of 1.7–2.1 eV to enable the red light to transmit, whereas the bottom-cell absorber should have a narrow bandgap of 1.0–1.4 eV to ensure that the red light can be absorbed.^[6] According to the Shockley–Queisser theory, a maximum power

conversion efficiency (PCE) of $\approx 22\%$ is attainable for a CBTS ($E_g \approx 2 \text{ eV}$) single-junction solar cell; if CBTS could serve as a top cell in series with an Si ($E_g \approx 1.1 \text{ eV}$) bottom cell, the total PCE of the tandem device could be greatly boosted up to $\approx 34\%$, outperforming the single-junction solar cells.^[7]

CBTS is an intrinsic p-type semiconductor owing to Cu-deficiency,^[8] hence it requires an n-type partner material to form heterojunction for solar cell devices. As shown in **Figure 1**, CBTS has a very large lattice constant; therefore, it is dif-

ficult to find suitable heteropartner materials to make ideally lattice-matched junctions. Misfit dislocations may produce dangling and wrong bonds at the interface that may create deep trap states. Via these trap levels, the photogenerated holes and electrons can recombine at the heterointerface, which could be even more detrimental to open-circuit voltages (V_{OC} 's) than recombination in the absorber bulk for wide-bandgap solar cells.^[9–11] Among the conventional buffer materials shown in **Figure 1**, CdS, with a bandgap $E_g \approx 2.4 \text{ eV}$, appears to show the smallest lattice mismatch with most of the absorbers. Also, with a suitable conduction band alignment to other absorbers and to transparent conductive oxides (TCOs), CdS is well known as a typical n-type heteropartner material, which is usually called the “buffer layer” in $\text{Cu}(\text{In,Ga})\text{Se}_2$ and CZTS solar cells or the “window layer” in CdTe solar cells.^[12,13] However, blue light with photon energies $E > 2.4 \text{ eV}$ is strongly absorbed by the CdS layer and so does not contribute to the photocurrents. This is evident by the reduction in the external quantum efficiency (EQE) with the spectral wavelength $\lambda < 520 \text{ nm}$ for most solar cell devices using a CdS buffer or window layer. Reducing the thickness of the CdS layer can minimize this absorption loss of blue light, but can increase the density of pin holes. The increased pin hole density may give rise to direct contact between the TCO front contact and the absorber layer, causing weak diodes and degrading device performance. An alternative approach is to increase the bandgap of CdS via reactively sputtering a CdS target in a mixed O_2/Ar environment. In addition to an increase in bandgap, oxygenation may cause a reduction in grain size and crystallinity, ultimately resulting in a nanocrystalline or even an amorphous film and a dramatic increase of the film resistivity.^[13–18] Notably, oxygenation can upshift the conduction band minimum (CBM) compared to that of CdS, keeping the electrons away from the Fermi level, which therefore serves to reduce the effective interface recombination rate

Dr. J. Ge, Dr. P. Koirala, C. R. Grice, Dr. P. J. Roland, Y. Yu, X. Tan, Prof. R. J. Ellingson, Prof. R. W. Collins, Prof. Y. Yan
Department of Physics and Astronomy & Wright Center for Photovoltaics Innovation and Commercialization
The University of Toledo
Toledo, Ohio 43606, United States
E-mail: Jie.Ge@UToledo.Edu; Yanfa.Yan@UToledo.edu



DOI: 10.1002/aenm.201601803

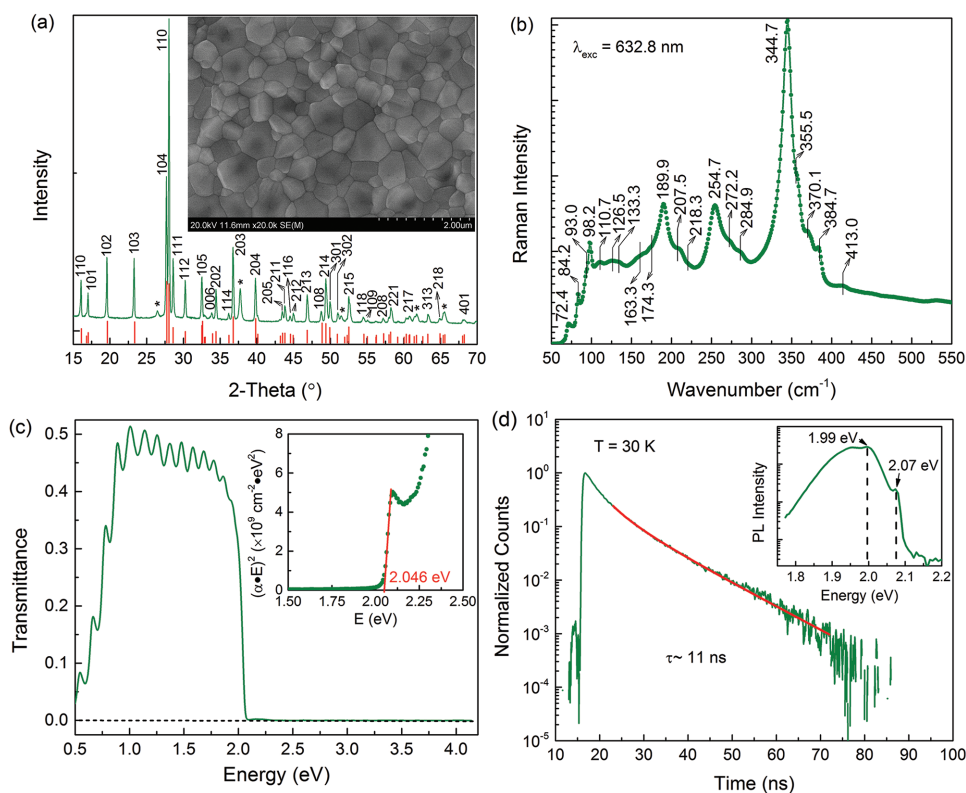


Figure 2. a) XRD pattern and top-view SEM image, b) Raman spectrum, c) optical transmission spectrum and bandgap plot, and d) 30 K photoluminescence (PL) spectrum and time-resolved PL (TRPL) recorded at 1.99 eV for a sulfurized CBTS film deposited on an FTO substrate. Note: XRD peaks marked by * in panel (a) at 2-Theta = 26.500°, 37.800°, 51.400°, 61.581°, and 65.540° correspond to the (110), (200), (211), (310), and (301) reflections of the FTO substrate (SnO₂, PDF 97-026-2768), respectively; the remaining XRD peaks in panel (a) are indexed to Cu₂BaSnS₄ (red markers, PDF 97-005-2685, space group P3₁); the absorption coefficient α in the inset of panel (c) was derived from the optical transmittance (T) and film thickness (d) based on the relation $\alpha = \frac{1}{d} \ln \frac{1}{T}$.

as expressed by Equation (S2) (Supporting Information), with the fitted parameters being given in Table S2 (Supporting Information). The imaginary part ϵ_2 suggests an absorption onset at ≈ 2.04 eV, consistent with the transmittance spectra (Figure 2c). The relative dielectric constant of CBTS $\epsilon_r \approx 5.4$ was obtained approximately by fitting the data for the real part ϵ_1 over the near-IR photon energy range applying a first-order Sellmeier equation.^[26] The result is consistent with the parametric high frequency dielectric constant $\epsilon_\infty \approx 5.3$. As shown in Figure 3b, CBTS exhibits a strong absorption coefficient, $\alpha > 10^4$ cm⁻¹ for the range of photon energies $E > 2$ eV. A plot of $(\alpha E)^2$ versus E based on SE-derived α in Figure 3b inset reveals the bandgap of CBTS at $E_g \approx 2.043$ eV, in a good agreement with the transmission results in Figure 2c. The CP analysis from the second derivatives of complex dielectric functions (Figure S3b, Supporting Information) yields a bandgap CP of $E_0 = 2.074$ eV with a broadening parameter of $\Gamma_0 = 0.094$ eV and seven other CPs above the bandgap at room temperature (Table S2, Supporting Information).^[27] Temperature-dependent SE measurements shown in panels (c) and (d) of Figure 3 reveal a characteristic redshift of the bandgap CP energy E_0 and an increase in CP broadening parameter Γ_0 with increasing temperature. As shown in Figure 3d, E_0 and Γ_0 vary linearly within the studied temperature range. The best linear fit leads to a temperature narrowing coefficient of -3.7×10^{-4} eV K⁻¹ for

CBTS bandgap. This result may enable precise measurement of the temperature during ongoing in situ deposition of CBTS over the temperature range studied.

CdS-based buffer layers were prepared by reactively sputtering a CdS target in the mixed O₂/Ar environment at ambient temperatures, whereby the O₂ contents (0%, 1%, 3%, 5%) were controlled by the flow ratio of O₂/Ar. Figure S3 (Supporting Information) shows the XRD patterns of these buffer layers deposited on soda lime glass substrates. CdS-based buffers sputtered using 0% and 1% O₂ exhibit multiple XRD peaks corresponding well to wurtzite CdS, suggesting that they are well crystalline; while, there is no specific XRD peaks observed in the CdS:O buffers sputtered using 3% and 5% O₂, suggesting the nanocrystalline or near amorphous crystalline structure. To identify the exact chemical component in our CdS:O buffers, X-ray photoelectron spectroscopy (XPS) measurements were conducted. XPS survey spectra in Figure S4a (Supporting Information) suggests that introducing O₂ in the sputtering environment results in a great density of oxygen being incorporated into the CdS:O buffers, which is evidenced by the intense O 1s peaks. A detailed measurement of the O 1s region (Figure S4b, Supporting Information) indicates that no significant Cd(OH)₂ and CdO_x species is present in CdS:O buffers.^[18,19,28] A detailed measurement of the S 2p region (Figure S4c, Supporting Information) indicates the presence of three sulfur species, namely

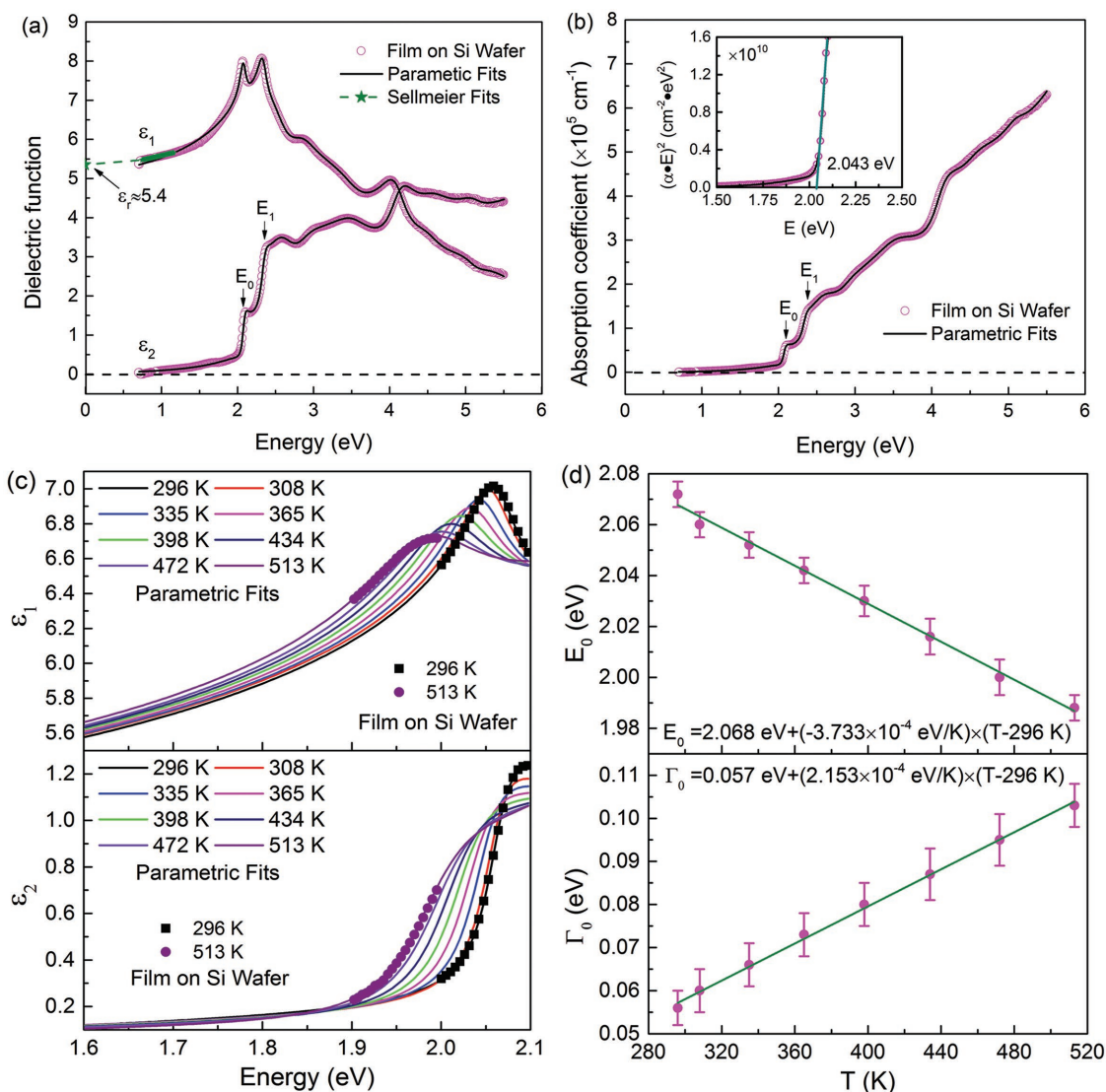


Figure 3. a) Real (ϵ_1) and imaginary (ϵ_2) parts of the dielectric function with a best parametric fit at room temperature, b) dielectric function derived absorption coefficient α and bandgap plot at room temperature, c) temperature-dependent real (ϵ_1) and imaginary (ϵ_2) parts of the dielectric function and their best parametric fits, d) temperature-dependent parametric bandgap critical point energies (E_0) and bandgap critical point broadening parameters (Γ_0) of a CBT film grown on a Si wafer measured by spectroscopic ellipsometry.

S^{2-} , SO_4^{2-} , and SO_3^{2-} ,^[17] suggesting that our sputtered CdS:O buffers consist of three components: CdS, CdSO₄, and CdSO₃. The component phase fractions can be further quantified by area percentages of the S 2p peaks from these three sulfur species. We find that the CdS:O buffer sputtered using 3% O₂ is comprised of 54.65% CdS, 26.41% CdSO₄, and 18.94% CdSO₃ and that the CdS:O buffer sputtered using 5% O₂ is comprised of 15.90% CdS, 72.13% CdSO₄, and 11.97% CdSO₃. This finding suggests that with increasing oxygenation, CdSO₄ is the preferred species in CdS:O buffers at the expense of CdS, whereas CdSO₃ content remains nearly unchanged.^[17,19] Although CdS:O exhibits the multiphase feature, there is only one apparent absorption edge observed in the optical transmission spectra (Figure S5a, Supporting Information). Hence, CdS:O bandgaps can be estimated at the vicinity of absorption edge based on the relation $(\alpha E)^2$ versus E . Figure S5b

(Supporting Information) shows that the plotted bandgap value increases from 2.42 eV for CdS to 3.70 eV for CdS:O sputtered using 5% O₂, leading to the film colour variance from yellow to transparent (Figure S5c, Supporting Information).

The flat band potential technique [i.e. Mott–Schottky (MS) plot] is a simple and low-cost method to determine the band positions and the carrier density of a photoelectrode material, which is widely used in photoelectrochemistry analysis.^[29] Herein, we employed this technique to evaluate CdS:O and CBTs. The n-type natures of CdS:O buffers are evidenced by the positive slopes of the measured MS plots shown in panels (a) and (b) of Figure S6 (Supporting Information). The linear-fit results of MS plots in Table S2 (Supporting Information) indicate that the CBM of CdS:O upshifts as oxygenation increases, while the carrier density decreases from 2×10^{18} to 8×10^{16} cm⁻³, consistent with the predications in the literature.^[13] The p-type

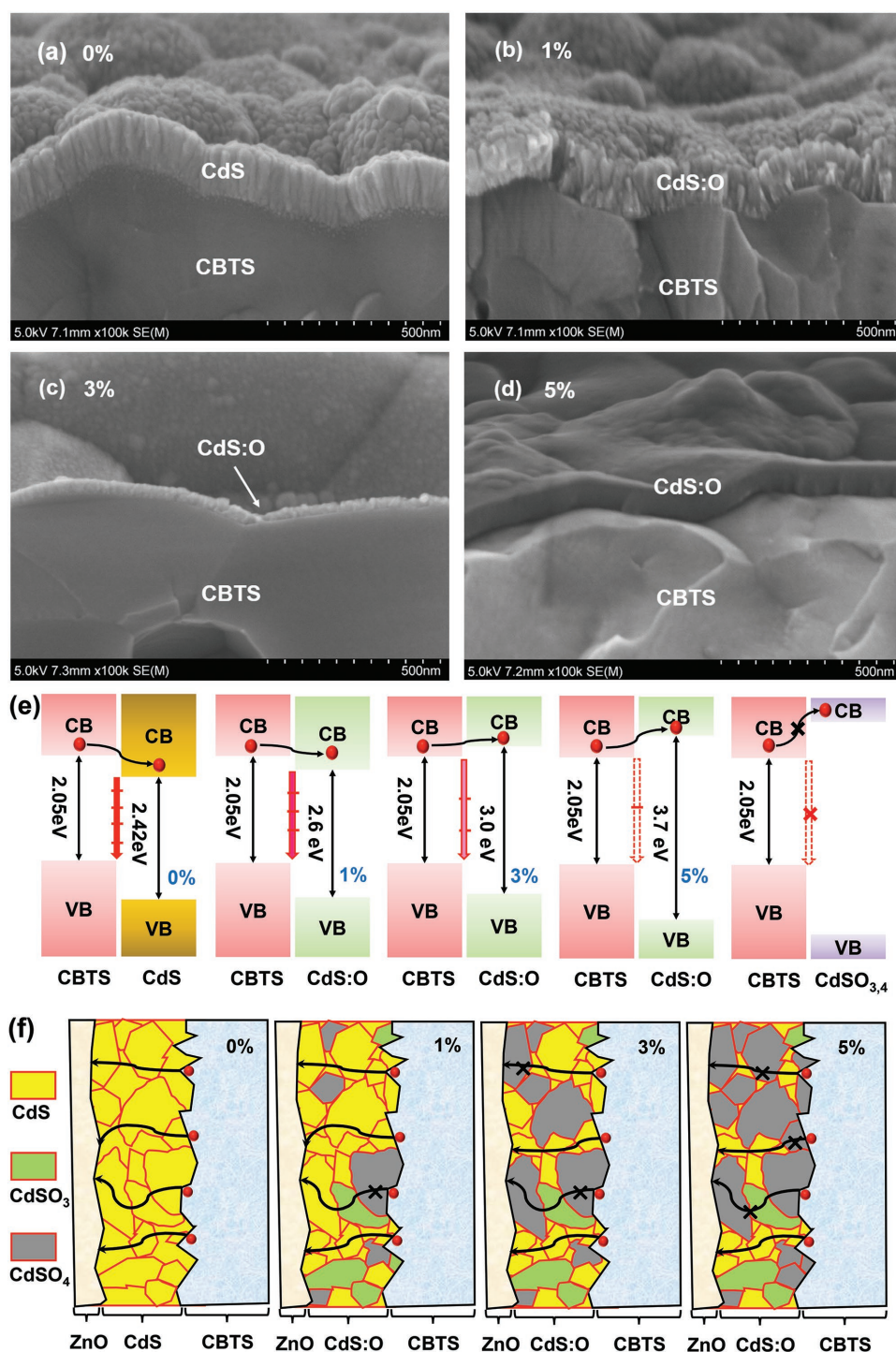


Figure 4. Cross-sectional SEM images of CBTS absorbers coated with CdS-based buffer layers reactively sputtered in the mixed O₂/Ar environment with a) 0%, b) 1%, c) 3%, and d) 5% O₂ at ambient temperatures, e) 1D band alignment sketches of CBTS/CdS, CBTS/CdS:O, and CBTS/CdSO_{3,4}, f) schematic representation of contact information of CdS:O buffers with CBTS absorbers. Note: in panel (e), CB-conduction band, VB-valence band; red arrows and red lines in panel (e) show recombination paths (red arrows) via interface defects (red lines); black arrows in panel (f) show that the passage of electrons from the CBTS layer is only permitted via conductive CdS phases, while insulating CdSO_{3,4} phases act as good passivators of the CBTS surface.

conductivity of CBTS is confirmed by the negative slope of the measured MS plot shown in Figure S6c (Supporting Information). The carrier density of CBTS was determined to be $0.5 \times 10^{16} \text{ cm}^{-3}$.

To create p–n junctions, CdS-based buffer layers were deposited on CBTS absorbers by reactively sputtering as described above. **Figure 4** shows the titled SEM images of the cross sections of CBTS films coated with sputtered CdS-based buffer

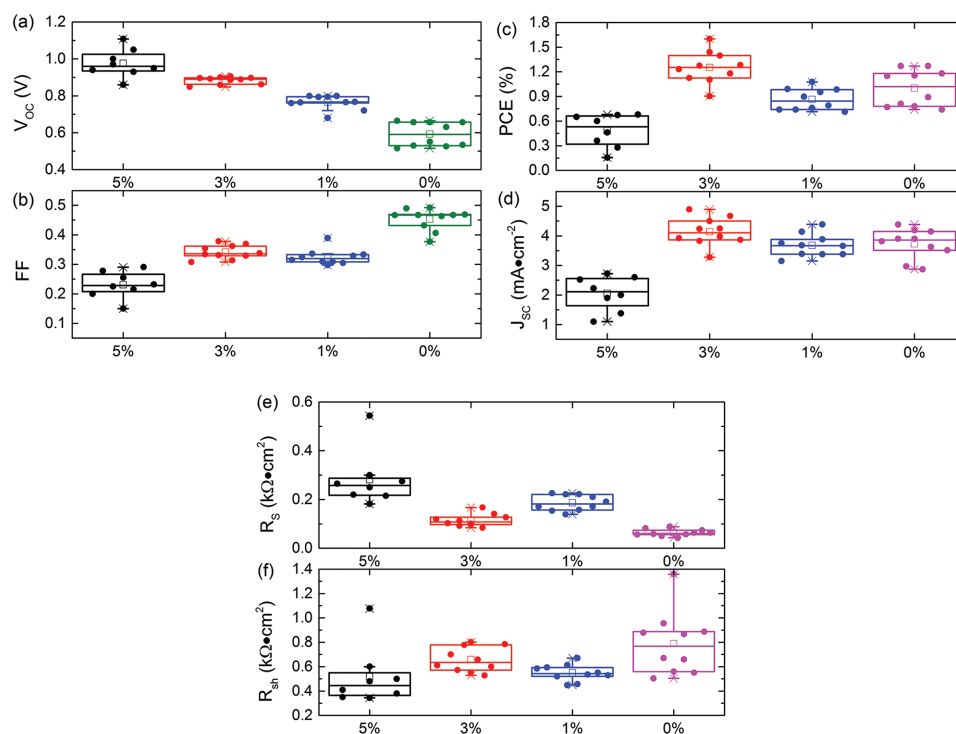


Figure 5. Statistical distribution of CBTS solar device parameters with the configuration FTO/CBTS/CdS-based buffer/ZnO/ZnO:Al, wherein CdS-based buffers were sputtered in the mixed O₂/Ar environment with varying O₂ contents (5%, 3%, 1%, 0%) at ambient temperatures: a) open circuit voltage (V_{OC}), b) fill factor (FF), c) power conversion efficiency (PCE), d) short circuit current (J_{SC}), e) series resistance (R_s), and f) shunt resistance (R_{sh}).

layers using different percentages of O₂. The CdS:O layer shown in Figure 3c was sputtered for ≈4 min whereas the others were sputtered for ≈11 min. As seen, CdS:O layers show dramatically reduced grain sizes with increased oxygenation, and 5% O₂ used in the sputtering environment eventually leads to an amorphous CdS:O buffer layer, consistent with the XRD observations in Figure S4 (Supporting Information). Followed by sequential deposits of sputtered intrinsic ZnO and aluminum-doped ZnO (ZnO:Al, front contact) overlayers, CBTS solar cells were constructed with the configuration FTO/CBTS/CdS-based buffer/ZnO/ZnO:Al.

Figure 5 shows the box charts of device parameters of these CBTS solar cells measured under AM 1.5G illumination from the ZnO:Al front contact. V_{OC} is quite an important photovoltaic parameter, being most directly affected by interface and bulk recombination.^[10] We observe that CBTS solar cells with CdS:O buffers show remarkably higher V_{OC} 's than CdS buffered cells, and V_{OC} 's continue to increase with higher oxygenation. This observation suggests that the dominant recombination for CdS buffered CBTS solar devices takes place at the heterojunction interface where holes from CBTS recombine with electrons from CdS, largely because of the conduction band misalignment and large lattice mismatch between CBTS and CdS. As shown in Figure S6d and Table S2 (Supporting Information), CdS buffer creates a cliff-like (type II) conduction band alignment with the CBTS absorber, that is, a CBM ≈0.57 V lower than that of CBTS, usually associated with higher interface recombination rates.^[9] In addition, the large lattice mismatch between CBTS and CdS may cause a high

density of interface defects, which can act as effective paths for carrier recombination at the heterojunction interface. As a result, interface recombination greatly limits the V_{OC} 's in CdS buffered cells, which are much less than the maximum attainable V_{OC} (≈1.65 V) for the absorber with a ≈2.0 eV bandgap based on the Shockley–Queisser limit. In contrast, the high V_{OC} 's observed in CdS:O buffered cells suggest interface recombination is greatly suppressed by using CdS:O buffer. First, nanocrystalline and amorphous CdS:O grains observed in panels (c) and (d) of Figure 4 can reduce the strain at the heterojunction and lessen the need for ideal lattice-matching junctions, thus facilitating a reduction in the density of interface defects and mitigating interface recombination.^[20] Second, the highly resistive CdSO₄ phase in CdS:O is known to be an effective passivator for interface defects. Thus the presence of CdSO₄ at CBTS surface is able to further minimize interface recombination.^[13,18] Likewise, CdSO₃ may likely play a similar role in surface passivation as does CdSO₄. Besides, CdS:O shows a higher CBM than CdS, which could move the electrons in the CdS:O buffer further away from the holes in CBTS, and therefore may greatly minimize interface recombination rates.^[13,30] As oxygenation increases, more CdSO₄ passivators form and the CBM of CdS:O shifts to higher energy as well.^[13,17,19] Thus, CdS:O buffers sputtered using higher O₂ contents enable higher V_{OC} 's by reducing interface recombination. The 1D band alignment roughly sketched in Figure 4e clearly delineates this situation, namely how well CdS:O improves V_{OC} 's in the presence of interface defects as compared to the results for CdS.

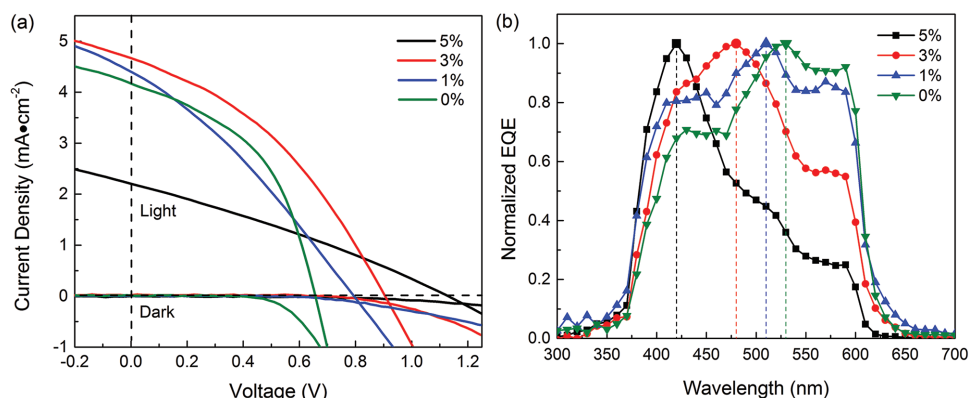


Figure 6. a) Light and dark J - V curves and b) normalized EQE curves of FTO/CBTS/CdS-based buffer/ZnO/ZnO:Al solar cell devices, wherein CdS-based buffer layers were reactively sputtered in the mixed O_2 /Ar environment with varying O_2 contents (5%, 3%, 1%, 0%) at ambient temperatures.

The champion V_{OC} of ≈ 1.1 V was achieved by the CdS:O buffer sputtered using 5% O_2 . But this CdS:O buffer leads to dramatically increased series resistances (R_s 's) as seen in Figure 5e. As has been proved by the XPS results in Figure S4 (Supporting Information), higher oxygenation will cause the formation of more $CdSO_4$ at the expense of CdS. Since $CdSO_4$ is electrically insulating, the current transport through the buffer layer will hinge on the CdS component in CdS:O.^[18] Therefore, the electron transport paths from CBTS are gradually reduced in CdS:O with the increase of oxygenation due to the formation of insulating $CdSO_4$ as illustrated in Figure 4f. As a result, oxygenation reduces the carrier density of CdS:O,^[13] greatly increases the film resistivity,^[14,15] and therefore increases the cell R_s 's. Eventually, the increased R_s 's dramatically degrade the FF's. Besides, this CdS:O buffer additionally yielded the lowest average short circuit current density (J_{SC}) (Figure 5d). The issue of low J_{SC} can be corroborated as a result of a spike-like (type I) conduction band alignment between CdS:O and CBTS, that is, the CBM of CdS:O is ≈ 0.56 V higher than that of CBTS as shown in Figure 4e. This large conduction band offset, $CBO = +0.56$ V, can act as a robust barrier for the electron transport from the CBTS to the front contact,^[13,30,31] even with the advantage of reducing interface recombination. Eventually, the low J_{SC} 's together with the low FF's, contribute to the low PCE's less than 1% as shown in Figure 5.

Figure 6a shows the J - V curves of typical CBTS solar cells in the configuration FTO/CBTS/CdS-based buffer/ZnO/ZnO:Al, wherein the CdS-based buffers were sputtered with varying O_2 contents at ambient temperatures. The corresponding device parameters are given in Table 1. The CdS:O buffer sputtered using 3% O_2 achieved the best CBTS solar cell with a PCE of 1.6%, a V_{OC} of ≈ 0.91 V, an FF of ≈ 0.38 , and a J_{SC} of ≈ 4.7 mA cm^{-2} , and

shows a CBM ≈ 0.28 V higher than that of CBTS. This slightly positive CBO = $+0.28$ V does not block the electron transports from the CBTS to the front contact; conversely, it can facilitate reducing interface recombination.^[13] Figure 6b shows the normalized EQE curves of these CdS:O buffered devices accordingly, where it can be observed that the EQE maxima shift from ≈ 2.4 to ≈ 3.0 eV with the increase of O_2 percentages. This blueshift of EQE maxima arises from the increased bandgap values of CdS:O buffers.

In order to improve FF's and J_{SC} 's and maintain high V_{OC} 's, reducing the thickness of CdS:O layer appears to be an effective solution,^[13,17] but this may increase the density of pin holes because it is challenging to deposit conformal overlayers by sputtering which are both uniform and ultrathin. As seen in Figure 4c, the sputtered CdS:O buffer with a thickness of ≈ 30 nm does not uniformly coat CBTS film without pin holes. The presence of pin holes may cause direct contacts between ZnO and CBTS and cause severe interface recombination. In this regard, we designed a bilayer buffer which includes an ultrathin CdS:O layer sputtered using 3% O_2 for ≈ 2 min plus a thicker layer of CdS sputtered in pure Ar for ≈ 5 min. This bilayer buffer design may form a favourable band alignment with CBTS for photocurrent extraction without sacrificing V_{OC} 's. Panels (a) and (b) of Figure 7 show the cross-sectional SEM images of a finished CBTS solar device with the configuration of FTO/CBTS/CdS:O/CdS/ZnO/ZnO:Al. The ≈ 2 μm thick CBTS absorber layer shows an equiaxed large-grain (>1 μm) microstructure with microvoids being observed at the film rear side (Figure 7a). As shown by the magnified SEM images in Figure 7b, there is no clear interface boundary between CdS:O and CdS layers, which is preferred to circumvent the parasitic interface recombination between CdS:O and CdS. As compared

Table 1. Device parameters of FTO/CBTS/CdS-based buffer/ZnO/ZnO:Al solar cell devices, wherein CdS-based buffers were reactively sputtered in the mixed O_2 /Ar environment with varying O_2 contents (5%, 3%, 1%, 0%) at ambient temperatures.

CdS:O	V_{OC} [V]	J_{SC} [mA cm^{-2}]	FF [%]	PCE [%]	R_s [Ω cm^2]	R_{sh} [Ω cm^2]
5%	1.108	2.22	27.77	0.68	183.00	343.60
3%	0.906	4.68	37.80	1.60	101.50	658.40
1%	0.795	4.39	30.86	1.08	139.34	449.45
0%	0.657	4.15	46.65	1.28	43.40	886.65

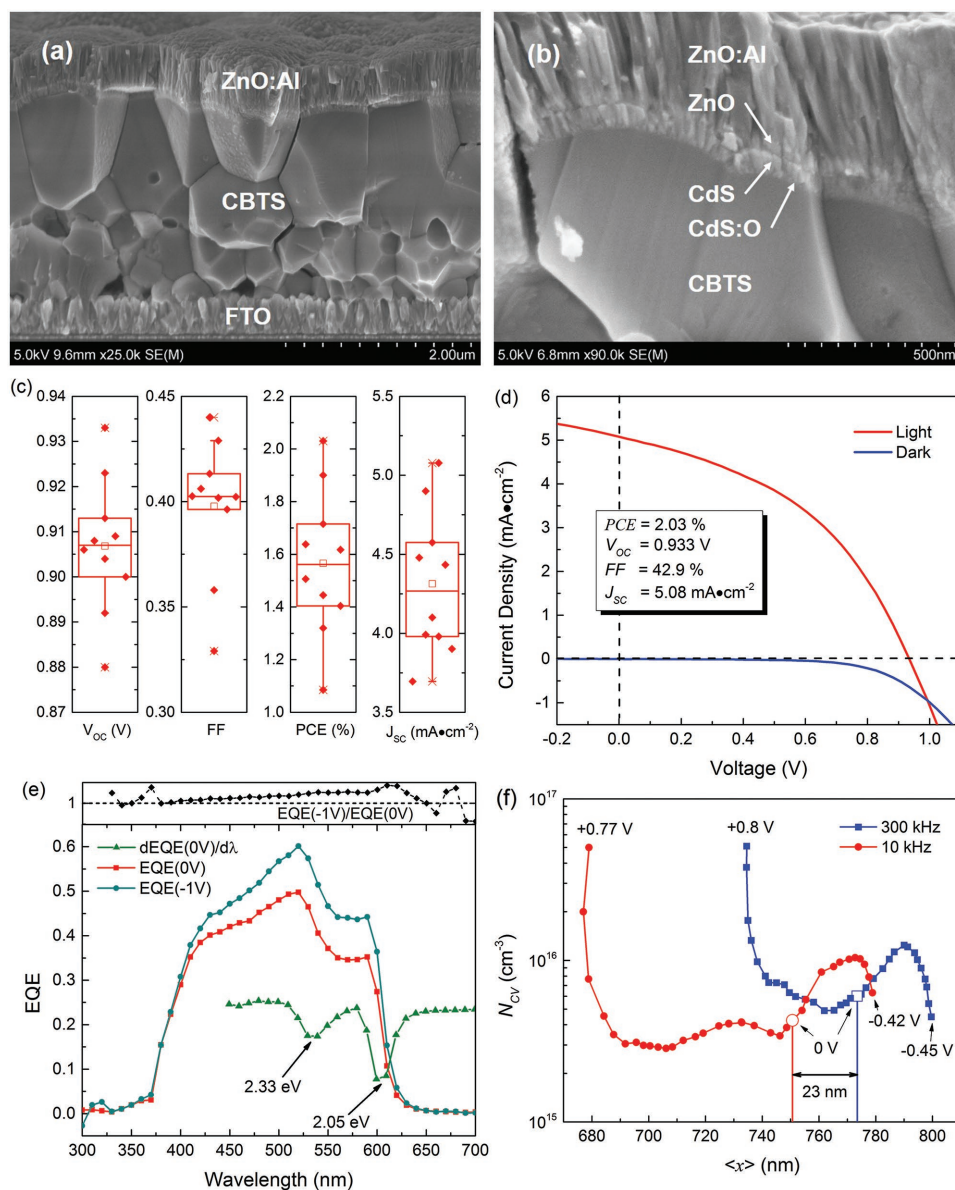


Figure 7. a) Cross-sectional SEM image of a finished CBTS solar cell with a configuration FTO/CBTS/CdS:O/CdS/ZnO/ZnO:Al, b) magnified SEM image showing the layer structure at the CBTS/CdS:O/CdS/ZnO interface region, c) statistical distribution of the device parameters of CBTS solar cells based on this bilayer buffer configuration, d) light and dark J - V curves, e) 0 and -1 V biased EQE curves, $dEQE/d\lambda$ versus wavelength λ curve, and the ratio of EQEs under -1 and 0 V, f) logarithmic representation of capacitance-voltage (C - V) derived carrier density profiles (N_{CV} versus $\langle x \rangle$) measured at 300 kHz and 10 kHz of our record CBTS solar device based on this bilayer buffer configuration. Note: the CdS:O layer was reactively sputtered using 3% O_2 plus 97% Ar at ambient temperatures.

to the device results based on the bare CdS:O buffer sputtered using 3% O_2 (Figure 5), this bilayer buffer achieves significantly improved FF's and slightly improved V_{OC} 's, both of which contribute to higher PCE's (Figure 7c).

Our best CBTS solar cell was achieved with this bilayer buffer and exhibited a PCE of 2.03% , a V_{OC} of 0.933 V, a FF of 0.43 , and a J_{SC} of 5.08 $mA\ cm^{-2}$ under AM 1.5G illumination from the ZnO:Al front contact (Figure 7d). The EQE spectra measured under reverse (-1 V) and zero biases of this record CBTS device are shown in Figure 7e. The integrated J_{SC} from the 0 V biased EQE, 5.2 $mA\ cm^{-2}$ (Figure S7, Supporting

Information), is consistent with that from the J - V measurement. Under a reverse bias, the depletion region extends into CBTS allowing more photogenerated carriers to be collected, resulting in an increased EQE as compared to the 0 V biased EQE. The ratio of EQE responses, in the form of $(-1\ V)/(0\ V)$, shows a gradual increase toward the longer wavelengths, indicating less collection of photocurrents at the rear side of CBTS. The inflection point of the 0 V biased EQE spectrum yields an absorption onset of 2.05 eV for the CBTS absorber, which is consistent with the values measured from UV-vis spectroscopy (Figure 2c inset), SE (Figure 3b inset) and the first

derivatives of the normalized EQE curves in Figure 6b (Figure S8, Supporting Information). The inflection point at 2.33 eV very likely derives from a higher energy CP (E_1) as denoted in panels (a) and (b) of Figure 3. The spatial carrier distribution of this record CBTS solar cell was characterized by capacitance–voltage ($C-V$) derived profiles of N_{CV} versus $\langle x \rangle$ as shown in Figure 7f, where $\langle x \rangle$ is the profiling distance from the junction. The $\langle x \rangle$ value of 751–774 nm at zero bias corresponds to the depletion region width of the CBTS solar cell, which is much less than the CBTS film thickness. As reverse biases were applied, the depletion region width was extended into the CBTS bulk region, allowing the carrier density of CBTS away from the junction region to be tested. N_{CV} profiles indicate that CBTS has a carrier density of $0.3\text{--}1.2 \times 10^{16} \text{ cm}^{-3}$, consistent with the values derived from the MS plot in Table S2 (Supporting Information). A rapid increase of N_{CV} at positive biases exceeding 0.7 V corresponds to the high carrier density in CdS. N_{CV} profiles measured at 300 kHz and 10 kHz additionally show a small profiling distance shift of $\Delta\langle x \rangle = 23 \text{ nm}$, suggesting no robust electrical barrier (either second diode or nonohmic contact) present in the device.^[32]

3. Conclusions

In this work, earth-abundant CBTS thin films were fabricated by postsulfurization of cosputtered sulfide precursors. Characterization measurements based on UV–vis spectroscopy, SE, Raman scattering, and $C-V$ profiles were conducted to acquire the fundamental physical parameters of CBTS, including optical absorption coefficient ($>10^4 \text{ cm}^{-1}$), band gap (2.04–2.07 eV), complex dielectric function, CPs for optical transitions, lattice vibrational modes, and carrier density ($\approx 10^{16} \text{ cm}^{-3}$). Temperature-dependent SE measurements additionally reveal that CBTS has a bandgap narrowing coefficient of $\approx -4 \times 10^{-4} \text{ eV K}^{-1}$ with increasing temperature. PL spectroscopy measurements suggest that the dominant defects in CBTS produce shallow energy levels.

CdS:O buffer layers were deposited on CBTS absorbers to create p–n junctions by reactively sputtering a CdS target in the mixed O_2/Ar environment. XPS measurements suggest that CdS:O is a mixture of CdS, CdSO_4 , and CdSO_3 . The V_{OC} 's of CBTS solar cells were enhanced through increased oxygenation in CdS:O buffers. A sputtered CdS:O buffer layer using 5% O_2 yielded the best V_{OC} of $\approx 1.1 \text{ V}$ among our CBTS solar cells; but this buffer greatly degraded the other device parameters as evidenced by large R_s 's, poor FF's, and small J_{SC} 's. Thus, the oxygen content in the sputtering environment and the thickness of CdS:O layer must be chosen with caution. In order to maintain high V_{OC} 's without sacrificing the other device parameters, a bilayered buffer was applied to the CBTS solar cells, which includes an ultrathin layer of sputtered CdS:O using 3% O_2 plus a thicker layer of sputtered CdS using pure Ar. This buffer design yielded our best-performing CBTS solar cell with a PCE of 2.03%, a V_{OC} of 0.93 V, an FF of 0.43, and a J_{SC} of 5.08 mA cm^{-2} .

This work demonstrates that CBTS is a promising earth-abundant material suitable as a top-cell absorber in tandem solar devices and also suggests that the optimization of interfacial contact

between CBTS and buffer layers is critical to V_{OC} enhancement. This work additionally opens a new area of wide bandgap photovoltaic materials within the trigonal and orthorhombic system of $(\text{Cu, Ag, Au})_2(\text{Sr, Ba, Eu})^{II}(\text{Ge, Sn})^{IV}(\text{S, Se})^{VI}_{4,}^{[1,5,33]}$ wherein none of the system members has gained much attention before.

Supporting Information

Supporting Information is available from the Wiley Online Library or from the author.

Acknowledgment

This work was supported by the National Science Foundation under contract no. CHE-1230246 and DMR-1534686, and Ohio Research Scholar Program. Weiwei Meng is thanked for his continuous supports in calculating the band structures of new quaternary chalcogenides.

Received: August 17, 2016

Revised: October 11, 2016

Published online:

- [1] C. L. Teske, O. Vetter, *Z. Anorg. Allg. Chem.* **1976**, 426, 281.
- [2] a) S. C. Abrahams, *Acta Crystallogr., Sect. B* **2003**, 59, 541; b) G. L. Schimek, W. T. Pennington, P. T. Wood, J. W. Kolis, *J. Solid State Chem.* **1996**, 123, 277.
- [3] F. Hong, W. Lin, W. Meng, Y. Yan, *Phys. Chem. Chem. Phys.* **2016**, 18, 4828.
- [4] D. Shin, B. Saparov, T. Zhu, W. P. Huhn, V. Blum, D. B. Mitzi, *Chem. Mater.* **2016**, 28, 4771.
- [5] J. Llanos, C. Mujica, V. c. Sánchez, O. Peña, *J. Solid State Chem.* **2003**, 173, 78.
- [6] a) S. Nishiwaki, S. Siebentritt, P. Walk, M. Ch. Lux-Steiner, *Prog. Photovoltaics* **2003**, 11, 243; b) T. Todorov, T. Gershon, O. Gunawan, C. Sturdevant, S. Guha, *Appl. Phys. Lett.* **2014**, 105, 173902; c) J. Werner, L. Barraud, A. Walter, M. Bräuninger, F. Sahli, D. Sacchetto, N. Tétreault, B. Paviet-Salomon, S.-J. Moon, C. Allebé, M. Despeisse, S. Nicolay, S. De Wolf, B. Niesen, C. Ballif, *ACS Energy Lett.* **2016**, 1, 474; d) Y. Liu, L. A. Renna, M. Bag, Z. A. Page, P. Kim, J. Choi, T. Emrick, D. Venkataraman, T. P. Russell, *ACS Appl. Mater. Interfaces* **2016**, 8, 7070; e) F. Lang, M. A. Gluba, S. Albrecht, J. Rappich, L. Korte, B. Rech, N. H. Nickel, *J. Phys. Chem. Lett.* **2015**, 6, 2745; f) T. Todorov, T. Gershon, O. Gunawan, Y. S. Lee, C. Sturdevant, L.-Y. Chang, S. Guha, *Adv. Energy Mater.* **2015**, 5, 1500799.
- [7] T. Todorov, O. Gunawan, S. Guha, *Mol. Syst. Des. Eng.* **2016**, DOI: 10.1039/C6ME00041J.
- [8] a) J. Ge, Y. Yu, Y. Yan, *J. Mater. Chem. A* **2016**, DOI: 10.1039/c6ta06702f; b) O. Mayasree, C. R. Sankar, K. M. Kleinke, H. Kleinke, *Coord. Chem. Rev.* **2012**, 256, 1377; c) J. Ge, Y. Yu, Y. Yan, *ACS Energy Lett.* **2016**, 1, 583.
- [9] Y. S. Lee, D. Chua, R. E. Brandt, S. C. Siah, J. V. Li, J. P. Mailoa, S. W. Lee, R. G. Gordon, T. Buonassisi, *Adv. Mater.* **2014**, 26, 4704.
- [10] M. Gloeckler, J. R. Sites, *Thin Solid Films* **2005**, 480–481, 241.
- [11] a) S. Chen, Y. Hou, H. Chen, M. Richter, F. Guo, S. Kahlmann, X. Tang, T. Stubhan, H. Zhang, N. Li, N. Gasparini, C. O. R. Quiroz, L. S. Khanzada, G. J. Matt, A. Osvet, C. J. Brabec, *Adv. Energy Mater.* **2016**, 6, 1600132; b) X. Zheng, B. Chen, M. Yang, C. Wu, B. Orler, R. B. Moore, K. Zhu, S. Priya, *ACS Energy Lett.* **2016**, 1, 424.

- [12] a) N. Naghavi, D. Abou-Ras, N. Allsop, N. Barreau, S. Bücheler, A. Ennaoui, C. H. Fischer, C. Guillen, D. Hariskos, J. Herrero, R. Klenk, K. Kushiya, D. Lincot, R. Menner, T. Nakada, C. Platzer-Björkman, S. Spiering, A. N. Tiwari, T. Törndahl, *Prog. Photovoltaics* **2010**, *18*, 411; b) J. Lindahl, J. T. Wätjen, A. Hultqvist, T. Ericson, M. Edoff, T. Törndahl, *Prog. Photovoltaics* **2013**, *21*, 1588.
- [13] J. M. Kephart, R. M. Geisthardt, W. S. Sampath, *Prog. Photovoltaics* **2015**, *23*, 1484.
- [14] X. Wu, Y. Yan, R. G. Dhere, Y. Zhang, J. Zhou, C. Perkins, B. To, *Phys. Status Solidi C* **2004**, *1*, 1062.
- [15] X. Wu, R. G. Dhere, Y. Yan, I. J. Romero, Y. Zhang, J. Zhou, C. DeHart, A. Duda, C. Perkins, B. To, presented at 29th IEEE Photovoltaic Specialists Conf., New Orleans, LA, May **2002**.
- [16] N. R. Paudel, C. R. Grice, C. Xiao, Y. Yan, *J. Appl. Phys.* **2014**, *116*, 044506.
- [17] D. M. Meysing, C. A. Wolden, M. M. Griffith, H. Mahabaduge, J. Pankow, M. O. Reese, J. M. Burst, W. L. Rance, T. M. Barnes, *J. Vac. Sci. Technol., A* **2015**, *33*, 021203.
- [18] K. Andreas, *J. Phys.: Condens. Matter* **2015**, *27*, 134201.
- [19] D. A. Duncan, J. M. Kephart, K. Horsley, M. Blum, M. Mezher, L. Weinhardt, M. Häming, R. G. Wilks, T. Hofmann, W. Yang, M. Bär, W. S. Sampath, C. Heske, *ACS Appl. Mater. Interfaces* **2015**, *7*, 16382.
- [20] J. M. Burst, J. N. Duenow, D. S. Albin, E. Colegrove, M. O. Reese, J. A. Aguiar, C. S. Jiang, M. K. Patel, M. M. Al-Jassim, D. Kuciauskas, S. Swain, T. Ablekim, K. G. Lynn, W. K. Metzger, *Nat. Energy* **2016**, *1*, 16015.
- [21] a) L. Gil-Escrig, A. Miquel-Sempere, M. Sessolo, H. J. Bolink, *J. Phys. Chem. Lett.* **2015**, *6*, 3743; b) T. Zhao, C.-C. Chueh, Q. Chen, A. Rajagopal, A. K. Y. Jen, *ACS Energy Lett.* **2016**, *1*, 757; c) C. F. J. Lau, X. Deng, Q. Ma, J. Zheng, J. S. Yun, M. A. Green, S. Huang, A. W. Y. Ho-Baillie, *ACS Energy Lett.* **2016**, *1*, 573; d) M. Kulbak, D. Cahen, G. Hodes, *J. Phys. Chem. Lett.* **2015**, *6*, 2452.
- [22] E. Kroumova, M. I. Aroyo, J. M. Perez-Mato, A. Kirov, C. Capillas, S. Ivantchev, H. Wondratschek, *Phase Transitions* **2003**, *76*, 155.
- [23] M. Himmrich, H. Haeuseler, *Spectrochim. Acta, Part A* **1991**, *47*, 933.
- [24] B. Ohnesorge, R. Weigand, G. Bacher, A. Forchel, W. Riedl, F. H. Karg, *Applied Physics Lett.* **1998**, *73*, 1224.
- [25] a) P. Koirala, J. Li, H. P. Yoon, P. Aryal, S. Marsillac, A. A. Rockett, N. J. Podraza, R. W. Collins, *Prog. Photovoltaics* **2016**, *24*, 1055; b) P. Aryal, A.-R. Ibdah, P. Pradhan, D. Attygalle, P. Koirala, N. J. Podraza, S. Marsillac, R. W. Collins, J. Li, *Prog. Photovoltaics* **2016**, *24*, 1200.
- [26] J. W. Gooch, in *Encyclopedic Dictionary of Polymers* (Ed: J. W. Gooch), Springer, New York, NY **2011**, p. 653.
- [27] R. W. Collins, A. S. Ferlauto, in *Handbook of Ellipsometry*, (Ed: E. A. Irene), William Andrew Publishing, Norwich, NY **2005**, p. 93.
- [28] D. W. Niles, G. Herdt, M. Al-Jassim, *J. Appl. Phys.* **1997**, *81*, 1978.
- [29] a) Z. Chen, T. G. Deutsch, H. N. Dinh, K. Domen, K. Emery, A. J. Forman, N. Gaillard, R. Garland, C. Heske, T. F. Jaramillo, A. Kleiman-Shwarsstein, E. Miller, K. Takane, J. Turner, in *Photoelectrochemical Water Splitting: Standards, Experimental Methods, and Protocols*, Springer, New York, NY **2013**, p. 63; b) A. Paracchino, N. Mathews, T. Hisatomi, M. Stefk, S. D. Tilley, M. Gratzel, *Energy Environ. Sci.* **2012**, *5*, 8673.
- [30] T. Song, A. Kanevce, J. R. Sites, *J. Appl. Phys.* **2016**, *119*, 233104.
- [31] T. Minemoto, T. Matsui, H. Takakura, Y. Hamakawa, T. Negami, Y. Hashimoto, T. Uenoyama, M. Kitagawa, *Sol. Energy Mater. Sol. Cells* **2001**, *67*, 83.
- [32] a) J. Ge, J. Chu, J. Jiang, Y. Yan, P. Yang, *ACS Appl. Mater. Interfaces* **2014**, *6*, 21118; b) J. Ge, J. Chu, Y. Yan, J. Jiang, P. Yang, *ACS Appl. Mater. Interfaces* **2015**, *7*, 10414.
- [33] a) C. L. Teske, *Z. Anorg. Allg. Chem.* **1976**, *419*, 67; b) J. Llanos, C. Mujica, A. Buljan, *J. Alloys Compd.* **2001**, *316*, 146; c) M. Tampier, D. Johrendt, *Z. Anorg. Allg. Chem.* **2001**, *627*, 312; d) A. Assoud, N. Soheilnia, H. Kleinke, *Chem. Mater.* **2005**, *17*, 2255; e) C. L. Teske, *Z. Anorg. Allg. Chem.* **1978**, *445*, 193; f) C. L. Teske, O. Vetter, *Z. Anorg. Allg. Chem.* **1976**, *427*, 200; g) C. L. Teske, *Z. Naturforsch.* **1979**, *34b*, 386.